A unified element stiffness matrix model for variable cross-section flexure hinges in compliant mechanisms for micro/nano positioning

Yanling Tian, Mingxuan Yang, Fujun Wang*, Chongkai Zhou, Xingyu Zhao, Dawei Zhang

Key Laboratory of Mechanism Theory and Equipment Design of Ministry of Education,

School of Mechanical Engineering, Tianjin University, Tianjin 300350, China

This paper presents a unified analytical model of element stiffness matrix for variable cross-section flexure hinges in plane deformation which is most frequently employed in planar-motion compliant mechanisms for micro/nano positioning. The unified analytical model is derived for flexure hinges in plane deformation based on the principle of virtual work. The derivation is generalized such that it can be applied to various geometries. To optimize and simplify element stiffness matrix model, four coefficients with curve integral are introduced. The results of the analysis were validated in part by modeling several previously investigated configurations, namely flexible beam hinge and right circular hinge. To further validate the proposed analytical model, finite element analysis and experimental testing were used. And the experimental testing shows the proposed unified model is more precise than pseudo-rigid-body method. The proposed model provides a concise and generalized solution to derive the element stiffness matrices of flexible hinges in plane deformation, which will have excellent applications in design and analysis of variable cross-section flexible hinges in compliant mechanisms.

1 Introduction

Flexure hinges are incorporated in a multitude of instruments and mechanisms used in precision positioning, micro/nano measurement and manufacture including atomic force microscope, scanning tunnel microscope, mask alignment system, etc (Tian et al. 2010; Qin et al. 2013; Wang et al. 2016; Qi et al. 2015; Bhagat et al. 2014). Traditional motor-ball-screw positioning system has a number of disadvantages, because it usually uses switching mechanisms to convert rotary motion to linear motion (Wang et al. 2015; Xiao et al. 2016; Guo et al. 2016; Cai et al. 2016; Wang et al. 2016; Wang et al. 2015). Due to the advantages of no friction, no backlash and no lubrication, flexible hinges are widely utilized in compliant mechanisms to produce accurate motion. Actually, flexible hinges in planar-motion compliant mechanisms respond as complex springs that react to in-plane axial load, shear load and

bending moment. The element stiffness matrices model of flexure hinges can investigate overall elastic properties, which is essential to predict the motion of compliant mechanisms.

Early works were directed towards the derivation of element stiffness matrices or element flexibility matrices for flexible hinges. Using the theory of mechanics of materials, Smith et al. (1997) developed the closed-form equations for symmetric single-axis semi-elliptical flexure hinges, indicating that the performance of elliptical flexure hinges is within the range constrained by circular flexure hinges and leaf flexure hinges in terms of stiffness. Lobontiu et al. (2001) derived an element flexibility matrix model for corner-filleted flexure hinges using Castigliano's second theorem, proving that performance of corner-filleted flexure hinges is within the domain confined by right circular flexure hinges and leaf flexure hinges in term of compliance. Lin et al. (2013) designed and analyzed a kind of hybrid flexure hinge composed of half a hyperbolic flexure hinge and half a corner-filleted flexure hinge. They studied various corner-filleted flexure hinges with some specific shapes and offered substantial essential numerical results on in- and out-of-plane stiffness and compliance to model the element stiffness matrices of flexure hinges. Some researchers attempted to derive a relatively unified model of element stiffness matrices or element flexibility matrices for flexible hinges. Chuan et al. (2014) investigated the element stiffness matrix with approximation to second order for Timoshenko beam with variable cross-section based on the principle of potential energy. Lignola et al. (2017) obtained an exact stiffness matrix model of two nodes Timoshenko beam on elastic medium by dealing with a generalized method to obtain a closed-form analytical solution for bending of a shear deformable beam resting on elastic medium. Unfortunately, these obtained models of element stiffness matrices or element flexibility matrices are complex, and thus limit their applications. In addition, some derived element stiffness matrices or element flexibility matrices are approximated, which assume structural bending deflection is cubic polynomial (Brown et al. 1984; Marotta et al. 2018). Therefore, it is essential to achieve a precise and concise unified analytical model for the design and analysis of variable cross-section flexible hinges configurations.

Based on the principle of virtual work, this paper presents a unified element stiffness matrix model for variable

cross-section flexure hinges in plane deformation with end loads in compliant mechanisms. The flexure longitudinal profile is defined by any continuous curve which renders the resulting unified model general. This variable cross-section flexure hinge is general in itself because in several limiting cases, and its geometry approaches that of previously analyzed configurations, such as the constant cross section, right circular, right elliptical, or right circular corner-filleted hinges. Four coefficients with curve integral are introduced to optimize and simplify the unified model. To validate the model, several specific configurations were analyzed. Finite element analysis (FEA) and experimental testing were used for further analysis.

2 The unified element stiffness matrix model

2.1 The general model for elastic deformations under loads

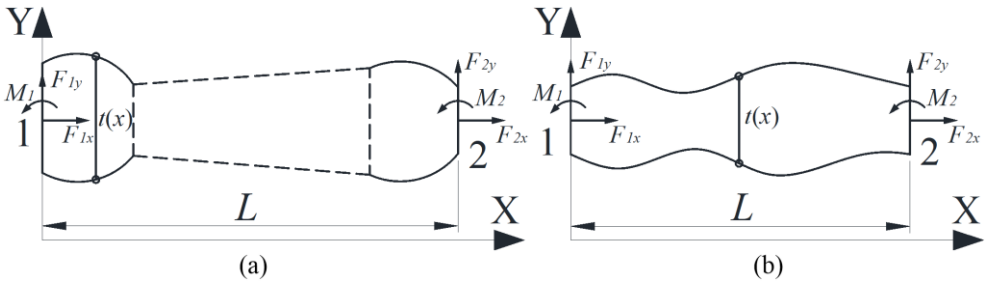

Fig. 1 The hinge model with end loads: **a** Multi-stage structure; **b** Single-segment structure

Considering flexure hinges in compliant mechanisms usually have relatively large width w compared to the variable thickness $t(x)$, which are designed to sustain in-plane deformations. And $t(x)$ is a function defined by the geometric profiles of flexure hinges. For flexure hinge model of Fig. 1 with constant width w and variable thickness $t(x)$, the general model for elastic deformations under loads can be derived from the principle of virtual work (Long et al. 2000):

$$\Delta = \sum\int \frac{\overline{M}M_P}{EI}ds + \sum\int \frac{\overline{F_N}F_{NP}}{EA}ds + \sum\int \frac{k\overline{F_Q}F_{QP}}{GA}ds \tag{1}$$

Eq. (1) is based on small deformation conditions. In Fig. 4, M_P, F_{NP} and F_{QP} represent the internal forces

caused by actual loads; $\overline{M}$, $\overline{F_N}$ and $\overline{F_Q}$ are the internal forces caused by virtual unit load; A represents the cross-section area; I is the cross-sectional moment of area; E is Young's modulus; G is shear modulus; k is the form factor and is equal to 1.2 when the cross section is rectangular.

2.2 The unified element stiffness matrix model

In order to illustrate the further work, it is necessary to specify the generalized hinge model used. For a flexure hinge in Fig. 1, the arc length, area and inertia moment of rectangular cross-section are $s = s(x)$ (generally, $s(x) = x$), $A(x) = wt(x)$ and $I = wt^3(x)/12$, where x is the abscissa. As Fig. 2a indicates, the left-end loads and displacements of the flexure hinge are F_{1x}, F_{1y}, M_1, u_1, v_1 and φ_1, and the right-end loads and displacements are F_{2x}, F_{2y}, M_2, u_2, v_2 and φ_2. For a flexible hinge of Fig. 2b with one end fixed and the other free, but under the action of F_{1x}, F_{1y} and M_1, the free-end displacements can be calculated by Eq. (1):

$$\Delta = \sum_{i=1}^{n}\int_{l_i}\frac{\overline{M}M_P}{EI(s)}ds + \sum_{i=1}^{n}\int_{l_i}\frac{\overline{F_N}F_{NP}}{EA(s)}ds + \sum_{i=1}^{n}\int_{l_i}\frac{k\overline{F_Q}F_{QP}}{GA(s)}ds \tag{2}$$

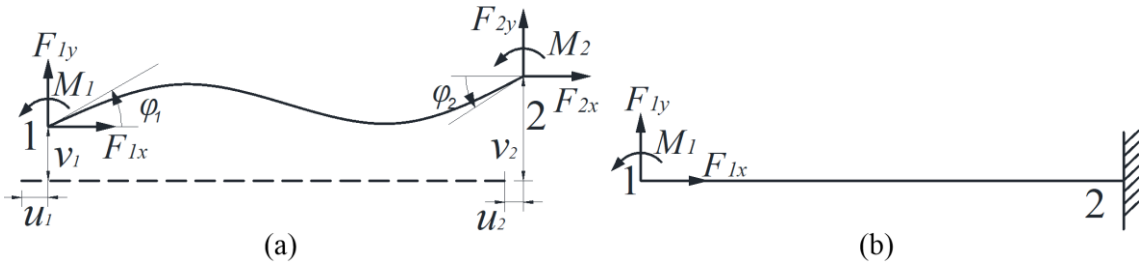

Fig. 2 Simplified model: **a** Loads and displacements configuration; **b** Simplified model

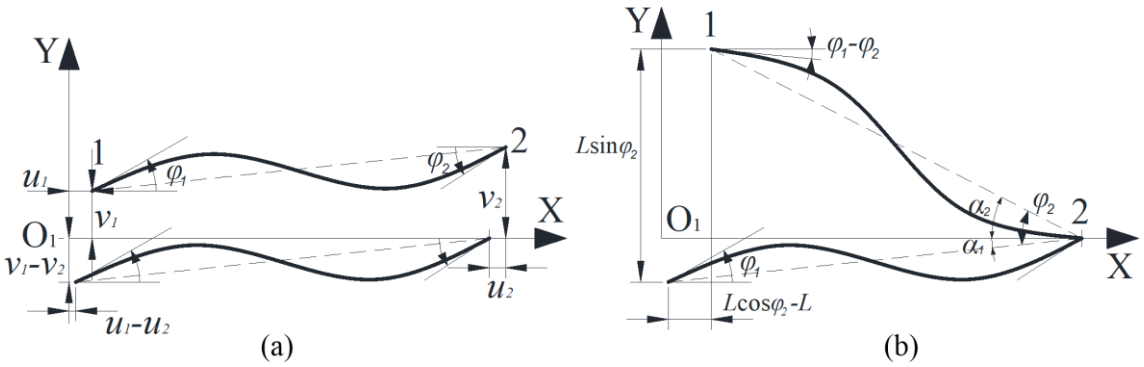

Fig. 3 Transformation model: **a** Translation; **b** Rotation

Fig. 3 pictures the right end of the flexure hinge model can be equivalent to fixed after translation and rotation, and the following geometric relationships can be obtained:

$$\begin{cases} \alpha_1 + \alpha_2 = \varphi_2 \\ \Delta_u = u_1 - u_2 + L\cos\alpha_1 - L\cos\alpha_2 \\ \Delta_v = v_1 - v_2 + L\sin\alpha_1 + L\sin\alpha_2 \\ \Delta_\varphi = \varphi_1 - \varphi_2 \end{cases} \tag{3}$$

According to Taylor's formula, it can be derived that as $\varphi_2, \alpha_1, \alpha_2 \to 0$, $\cos\alpha_1 - \cos\alpha_2 = 0(\varphi_2)$, $\sin\alpha_1 + \sin\alpha_2 = \varphi_2 + 0(\varphi_2)$. Therefore, the left-end generalized displacements can be rewritten:

$$\begin{cases} \Delta_u = u_1 - u_2 \\ \Delta_v = v_1 - v_2 + L\varphi_2 \\ \Delta_\varphi = \varphi_1 - \varphi_2 \end{cases} \tag{4}$$

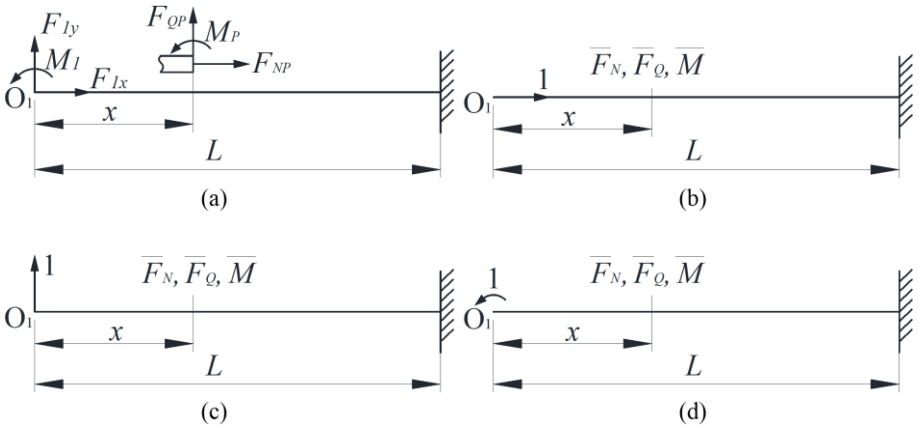

Fig. 4 The unit load method: **a** Actual load; **b** X-direction unit load; **c** Y-direction unit load; **d** θ_i-direction unit load

Next, the free-end displacements of the flexure hinge model can be calculated by Eq. (2). The left endpoint taken as the coordinate origin of the local reference frame XO_1Y in Fig. 4a, the internal forces caused by actual loads can be calculated as

$$\begin{cases} F_{NP} = -F_{1x} \\ F_{QP} = F_{1y} \\ M_P = -M_1 + F_{1y}x \end{cases}, x \in (0, L) \tag{5}$$

As shown in Fig. 4b, the internal forces caused by X-direction virtual unit load and the corresponding left-end

generalized displacement can be written as

$$\begin{cases} \overline{F_N} = -1 \\ \overline{F_Q} = 0 \ , x \in (0, L) \\ \overline{M} = 0 \end{cases} \tag{6}$$

$$\Delta_u = u_1 - u_2 = \sum_{i=1}^{n} \int_{l_i} \frac{1}{EA(s)} ds F_{1x} \tag{7}$$

As indicated in Fig. 4c, the internal forces caused by Y-direction virtual unit load and the corresponding left-end generalized displacement can be formulated as

$$\begin{cases} \overline{F_N} = 0 \\ \overline{F_Q} = 1 \, , x \in (0, L) \\ \overline{M} = x \end{cases} \tag{8}$$

$$\Delta_v = v_1 - v_2 + L\varphi_2 = -\sum_{i=1}^{n} \int_{l_i} \frac{x}{EI(s)} ds M_1 + \left(\sum_{i=1}^{n} \int_{l_i} \frac{x^2}{EI(s)} ds + \sum_{i=1}^{n} \int_{l_i} \frac{k}{GA(s)} ds \right) F_{1y} \tag{9}$$

As shown in Fig. 4d, the internal forces caused by θ_z -direction virtual unit load and the corresponding left-end generalized displacement can be expressed as

$$\begin{cases} \overline{F_N} = 0 \\ \overline{F_Q} = 0 \ , x \in (0, L) \\ \overline{M} = -1 \end{cases} \tag{10}$$

$$\Delta_\varphi = \varphi_1 - \varphi_2 = \sum_{i=1}^{n} \int_{l_i} \frac{1}{EI(s)} ds M_1 - \sum_{i=1}^{n} \int_{l_i} \frac{x}{EI(s)} ds F_{1y} \tag{11}$$

Four coefficients with curve integral were defined as following:

$$\begin{cases} \eta = \sum_{i=1}^{n} \int_{l_i} \frac{1}{EA(s)} ds \\ \lambda_0 = \sum_{i=1}^{n} \int_{l_i} \frac{1}{EI(s)} ds \\ \lambda_1 = \sum_{i=1}^{n} \int_{l_i} \frac{x}{EI(s)} ds \\ \lambda_2 = \sum_{i=1}^{n} \int_{l_i} \frac{x^2}{EI(s)} ds + \sum_{i=1}^{n} \int_{l_i} \frac{k}{GA(s)} ds \end{cases} , x \in (0, L) \tag{12}$$

The following matrix equations can be obtained from Eq. (7), (9) and (11):

$$\begin{bmatrix} \eta & 0 & 0 \\ 0 & \lambda_2 & -\lambda_1 \\ 0 & -\lambda_1 & \lambda_0 \end{bmatrix} \begin{bmatrix} F_{1x} \\ F_{1y} \\ M_1 \end{bmatrix} = \begin{bmatrix} 1 & 0 & 0 & -1 & 0 & 0 \\ 0 & 1 & 0 & 0 & -1 & L \\ 0 & 0 & 1 & 0 & 0 & -1 \end{bmatrix} \begin{bmatrix} u_1 \\ v_1 \\ \varphi_1 \\ u_2 \\ v_2 \\ \varphi_2 \end{bmatrix} \tag{13}$$

$$\begin{bmatrix} F_{1x} \\ F_{1y} \\ M_1 \end{bmatrix} = \begin{bmatrix} \frac{1}{\eta} & 0 & 0 & -\frac{1}{\eta} & 0 & 0 \\ 0 & \frac{\lambda_0}{\lambda_0\lambda_2-\lambda_1^2} & \frac{\lambda_1}{\lambda_0\lambda_2-\lambda_1^2} & 0 & \frac{-\lambda_0}{\lambda_0\lambda_2-\lambda_1^2} & \frac{-\lambda_1+L\lambda_0}{\lambda_0\lambda_2-\lambda_1^2} \\ 0 & \frac{\lambda_1}{\lambda_0\lambda_2-\lambda_1^2} & \frac{\lambda_2}{\lambda_0\lambda_2-\lambda_1^2} & 0 & \frac{-\lambda_1}{\lambda_0\lambda_2-\lambda_1^2} & \frac{-\lambda_2+L\lambda_1}{\lambda_0\lambda_2-\lambda_1^2} \end{bmatrix} \begin{bmatrix} u_1 \\ v_1 \\ \varphi_1 \\ u_2 \\ v_2 \\ \varphi_2 \end{bmatrix} \tag{14}$$

There is an obvious balance relationship:

$$\begin{bmatrix} F_{2x} \\ F_{2y} \\ M_2 \end{bmatrix} = \begin{bmatrix} -1 & 0 & 0 \\ 0 & -1 & 0 \\ 0 & L & -1 \end{bmatrix} \begin{bmatrix} F_{1x} \\ F_{1y} \\ M_1 \end{bmatrix} \tag{15}$$

By Eq. (14) and (15), the following equation can be derived:

$$\begin{bmatrix} F_{1x} \\ F_{1y} \\ M_1 \\ F_{2x} \\ F_{2y} \\ M_2 \end{bmatrix} = \begin{bmatrix} \frac{1}{\eta} & 0 & 0 & -\frac{1}{\eta} & 0 & 0 \\ 0 & \frac{\lambda_0}{\lambda_0\lambda_2-\lambda_1^2} & \frac{\lambda_1}{\lambda_0\lambda_2-\lambda_1^2} & 0 & \frac{-\lambda_0}{\lambda_0\lambda_2-\lambda_1^2} & \frac{-\lambda_1+L\lambda_0}{\lambda_0\lambda_2-\lambda_1^2} \\ 0 & \frac{\lambda_1}{\lambda_0\lambda_2-\lambda_1^2} & \frac{\lambda_2}{\lambda_0\lambda_2-\lambda_1^2} & 0 & \frac{-\lambda_1}{\lambda_0\lambda_2-\lambda_1^2} & \frac{-\lambda_2+L\lambda_1}{\lambda_0\lambda_2-\lambda_1^2} \\ -\frac{1}{\eta} & 0 & 0 & \frac{1}{\eta} & 0 & 0 \\ 0 & \frac{-\lambda_0}{\lambda_0\lambda_2-\lambda_1^2} & \frac{-\lambda_1}{\lambda_0\lambda_2-\lambda_1^2} & 0 & \frac{\lambda_0}{\lambda_0\lambda_2-\lambda_1^2} & \frac{\lambda_1-L\lambda_0}{\lambda_0\lambda_2-\lambda_1^2} \\ 0 & \frac{-\lambda_1+L\lambda_0}{\lambda_0\lambda_2-\lambda_1^2} & \frac{-\lambda_2+L\lambda_1}{\lambda_0\lambda_2-\lambda_1^2} & 0 & \frac{\lambda_1-L\lambda_0}{\lambda_0\lambda_2-\lambda_1^2} & \frac{\lambda_2-2L\lambda_1+L^2\lambda_0}{\lambda_0\lambda_2-\lambda_1^2} \end{bmatrix} \begin{bmatrix} u_1 \\ v_1 \\ \varphi_1 \\ u_2 \\ v_2 \\ \varphi_2 \end{bmatrix} \tag{16}$$

The element stiffness matrix can be written:

$$\boldsymbol{K}^{e}=\begin{bmatrix}
\frac{1}{\eta} & 0 & 0 & -\frac{1}{\eta} & 0 & 0 \\
0 & \frac{\lambda_0}{\lambda_0\lambda_2-\lambda_1^2} & \frac{\lambda_1}{\lambda_0\lambda_2-\lambda_1^2} & 0 & \frac{-\lambda_0}{\lambda_0\lambda_2-\lambda_1^2} & \frac{-\lambda_1+L\lambda_0}{\lambda_0\lambda_2-\lambda_1^2} \\
0 & \frac{\lambda_1}{\lambda_0\lambda_2-\lambda_1^2} & \frac{\lambda_2}{\lambda_0\lambda_2-\lambda_1^2} & 0 & \frac{-\lambda_1}{\lambda_0\lambda_2-\lambda_1^2} & \frac{-\lambda_2+L\lambda_1}{\lambda_0\lambda_2-\lambda_1^2} \\
-\frac{1}{\eta} & 0 & 0 & \frac{1}{\eta} & 0 & 0 \\
0 & \frac{-\lambda_0}{\lambda_0\lambda_2-\lambda_1^2} & \frac{-\lambda_1}{\lambda_0\lambda_2-\lambda_1^2} & 0 & \frac{\lambda_0}{\lambda_0\lambda_2-\lambda_1^2} & \frac{\lambda_1-L\lambda_0}{\lambda_0\lambda_2-\lambda_1^2} \\
0 & \frac{-\lambda_1+L\lambda_0}{\lambda_0\lambda_2-\lambda_1^2} & \frac{-\lambda_2+L\lambda_1}{\lambda_0\lambda_2-\lambda_1^2} & 0 & \frac{\lambda_1-L\lambda_0}{\lambda_0\lambda_2-\lambda_1^2} & \frac{\lambda_2-2L\lambda_1+L^2\lambda_0}{\lambda_0\lambda_2-\lambda_1^2}
\end{bmatrix} \tag{17}$$

Equation (17) is the unified element stiffness matrix model for variable cross-section flexure hinges in plane deformation with end loads, with coefficients η, λ_0, λ_1 and λ_2 related to the geometric configurations and material constants. With one end fixed and the other free, as illustrated in Fig. 2b, the unified element stiffness matrix model for variable cross-section flexure hinges in plane deformation can be written:

$$\boldsymbol{K}^{e}=\begin{bmatrix}
\frac{1}{\eta} & 0 & 0 \\
0 & \frac{\lambda_0}{\lambda_0\lambda_2-\lambda_1^2} & \frac{\lambda_1}{\lambda_0\lambda_2-\lambda_1^2} \\
0 & \frac{\lambda_1}{\lambda_0\lambda_2-\lambda_1^2} & \frac{\lambda_2}{\lambda_0\lambda_2-\lambda_1^2}
\end{bmatrix} \tag{18}$$

2.3 The unified element flexibility matrix model

For a flexure hinge model in plane deformation with one end fixed and the other free, as shown in Fig. 2b, the fixed-end displacement is zero, and Eq. (13) can be simplified as

$$\begin{bmatrix}\eta & 0 & 0\\ 0 & \lambda_2 & -\lambda_1\\ 0 & -\lambda_1 & \lambda_0\end{bmatrix}\begin{bmatrix}F_{1x}\\ F_{1y}\\ M_1\end{bmatrix}=\begin{bmatrix}u_1\\ v_1\\ \varphi_1\end{bmatrix} \tag{19}$$

Equation (19) can be also written as

$$\begin{bmatrix}u\\ v\\ \varphi\end{bmatrix}=\begin{bmatrix}\eta & 0 & 0\\ 0 & \lambda_2 & -\lambda_1\\ 0 & -\lambda_1 & \lambda_0\end{bmatrix}\begin{bmatrix}F_{1x}\\ F_{1y}\\ M_1\end{bmatrix} \tag{20}$$

Where $[F_{1x}, F_{1y}, M_1]^{\mathrm{T}}$ is left-end load and $[u, v, \varphi]^{\mathrm{T}}$ is the corresponding left-end displacement.

The united element flexibility matrix model for variable cross-section flexure hinges in plane deformation with one end fixed can be obtained:

$$\boldsymbol{C}^{e}=\begin{bmatrix}\eta & 0 & 0\\ 0 & \lambda_2 & -\lambda_1\\ 0 & -\lambda_1 & \lambda_0\end{bmatrix} \tag{21}$$

The element flexibility matrix (Eq. (21)) is the inverse matrix of the element stiffness matrix (Eq. (18)) and is consistent with the results in reference (Lobontiu et al. 2014).

3 Applications of the unified model

The general flexure hinge model can reduce to the constant section flexible beam, the right circular design, or the right elliptical configuration, which is particularly useful for validation purposes and allows for the comparison of modeling element stiffness matrix of some obtained model in previous studies. For practical convenience of the limit calculations, the element stiffness matrices of some specific common flexure hinges are obtained by the unified element stiffness matrix model (Eq. (17)). To validate the unified model (Eq. (17)), material Poisson's ratio is set as: $\mu=0.33$, the geometric dimensions are described and the coefficients η, λ_0, λ_1, λ_2 and λ_{2S} (represents the simplified algorithm of λ_2) are calculated in the following hinge models.

$$\lambda_{2S}=\sum_{i=1}^{n}\int_{l_i}\frac{x^2}{EI(s)}ds, x\in(0,L) \tag{22}$$

3.1 Constant section flexible beam hinge

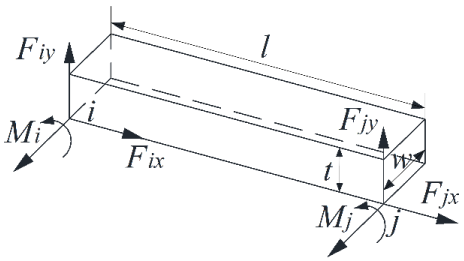

Fig. 5 Constant section flexible beam

Table 1 Coefficients calculation results

η	λ_0	λ_1	λ_2	λ_{2S}
$\frac{l}{EA}$	$\frac{l}{EI}$	$\frac{\frac{1}{2}l^2}{EI}$	$\frac{\frac{1}{3}l^3}{EI}+\frac{kl}{GA}$	$\frac{\frac{1}{3}l^3}{EI}$

As pictured in Fig. 5, considering flexible beam hinges in mechanisms usually satisfy $t/l \le 1/10$, it can be derived:

$$(\lambda_2\text{-}\lambda_{2S})/\lambda_{2S}=\int_0^L \frac{k}{GA(x)}dx \Big/ \int_0^L \frac{x^2}{EI(x)}dx = 0.6(1+\mu)\left(\frac{t}{l}\right)^2 \le 1\% \tag{23}$$

So λ_2 can be replaced by λ_{2S} . The element stiffness matrix and element flexibility matrix of the constant section flexible beam hinge can be obtained by substituting the coefficients η , λ_0 , λ_1 , λ_2 and λ_{2S} in Table 1 into Eq. (17) and (21). And equation (24) and (25) are consistent with the results in reference (Noveanu et al. 2015).

$$\boldsymbol{K}^e=\begin{bmatrix} \frac{EA}{l} & 0 & 0 & -\frac{EA}{l} & 0 & 0 \\ 0 & \frac{12EI}{l^3} & \frac{6EI}{l^2} & 0 & -\frac{12EI}{l^3} & \frac{6EI}{l^2} \\ 0 & \frac{6EI}{l^2} & \frac{4EI}{l} & 0 & -\frac{6EI}{l^2} & \frac{2EI}{l} \\ -\frac{EA}{l} & 0 & 0 & \frac{EA}{l} & 0 & 0 \\ 0 & -\frac{12EI}{l^3} & -\frac{6EI}{l^2} & 0 & \frac{12EI}{l^3} & -\frac{6EI}{l^2} \\ 0 & \frac{6EI}{l^2} & \frac{2EI}{l} & 0 & -\frac{6EI}{l^2} & \frac{4EI}{l} \end{bmatrix} \tag{24}$$

$$\boldsymbol{C}^e=\begin{bmatrix} \frac{l}{EA} & 0 & 0 \\ 0 & \frac{\frac{1}{3}l^3}{EI} & -\frac{\frac{1}{2}l^2}{EI} \\ 0 & -\frac{\frac{1}{2}l^2}{EI} & \frac{l}{EI} \end{bmatrix} \tag{25}$$

3.2 Right circular hinge

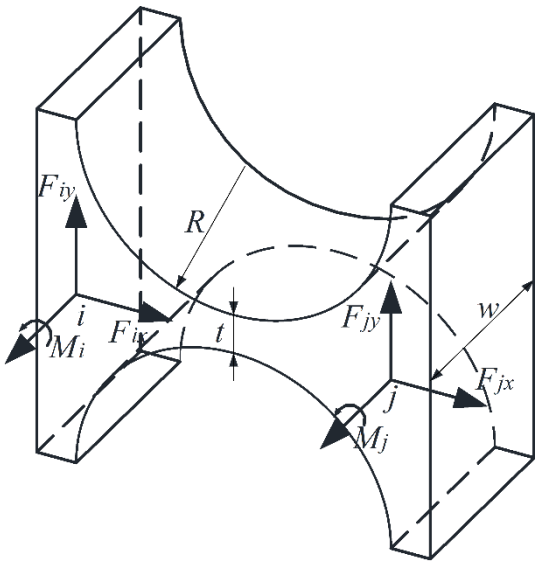

Fig. 6 Right circular hinge

Table 2 Coefficients calculation results

$t(x)$	$t+2r-2\sqrt{r^2-(r-x)^2}$
η	$\int_0^{\pi}\frac{R\sin\theta d\theta}{Eb\left(t+2R\left(1-\sin\theta\right)\right)}$
λ_0	$\int_0^{\pi}\frac{12R\sin\theta d\theta}{Eb\left(t+2R\left(1-\sin\theta\right)\right)^3}$
λ_1	$\int_0^{\pi}\frac{12R^2\left(1-\cos\theta\right)\sin\theta d\theta}{Eb\left(t+2R\left(1-\sin\theta\right)\right)^3}$
λ_2	$\int_0^{\pi}\frac{12R^3\left(1-\cos\theta\right)^2\sin\theta d\theta}{Eb\left(t+2R\left(1-\sin\theta\right)\right)^3}+\int_0^{\pi}\frac{kR\sin\theta d\theta}{Gb\left(t+2R\left(1-\sin\theta\right)\right)}$
λ_{2S}	$\int_0^{\pi}\frac{12R^3\left(1-\cos\theta\right)^2\sin\theta d\theta}{Eb\left(t+2R\left(1-\sin\theta\right)\right)^3}$

To investigate λ_2 simplified algorithm error, a nondimensional ratio $\alpha=t/R$ (usually, $\alpha\le 0.5$) and error $y(\alpha)$ were defined

$$y(\alpha)=(\lambda_2\text{-}\lambda_{2S})/\lambda_{2S}=\int_0^L\frac{k}{GA(x)}dx\Big/\int_0^L\frac{x^2}{EI(x)}dx \tag{26}$$

As Fig. 7 indicates, the curve $y = y(\alpha)$ can be drawn by Matlab software, indicating that $y \le 2\%$ when $\alpha \le 0.2$. Without requiring precise calculation, λ_2 can be replaced by λ_{2S}. By the coefficients summarized in Table II, the element stiffness matrix and element flexibility matrix of the right circular hinge can be obtained using the unified model (Eq. (17) and (21)). And the results are consistent with the results in references (Wang et al. 2008; Lobontiu et al. 2013).

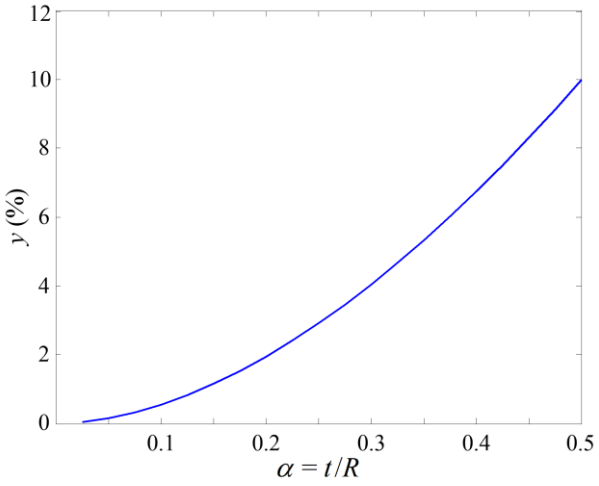

Fig. 7 The influence of the ratio α on calculation error of λ_2

4 Validation and analysis

In addition to limit calculation, finite element analysis and experimental testing were used to analyze and validate the unified element stiffness matrix model. ANSYS code was used to perform finite element analysis. And experimental testing of a special combined hinge was performed to investigate the application of the proposed unified model. The material constants were: Young's modulus $E = 70GPa$ and Poisson's ratio $\mu = 0.33$.

4.1 Finite element analysis

As shown in Fig. 8, to analysis the geometric parameters' influence on calculation error of the unified model, finite element analysis of a right circular hinge model formed of two constant cross-section segments and one right circular segment were performed, and its geometric parameters were: $w = 8mm$, $R = 2mm$, and $l_1 = 4mm$. Its min-thickness

t is designed as a set of values. In Fig. 8, the left-end face is under constant uniformly distributed loads, including surface loads X-direction load F_x^0, Y-direction load F_y^0 and θ_z-direction moment M^0 in global coordinate system, without any other constraint. And the right-end face is completely fixed in three-dimensional space, perpendicular to the X direction of global coordinate system. The nonlinear controls module was used to analysis nonlinear behavior. By FEA, when the deformation is small, two constant cross-section segments can be treated as rigid bodies, and it can be found that the instantaneous centre of rotation is always at the geometry center of the right circular segment ($error \le 10^{-9} m$).

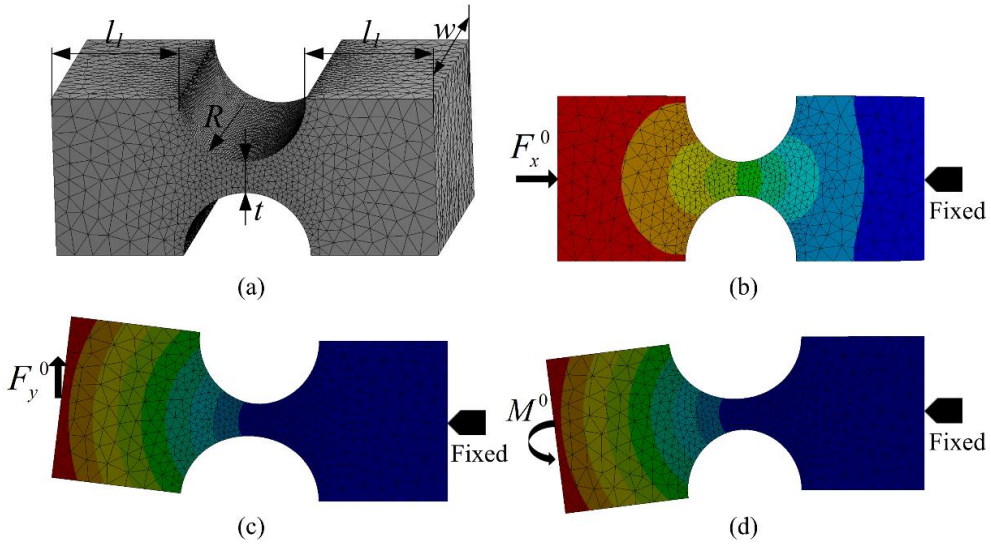

Fig. 8 FEA model of the right circular hinge: **a** Meshing model; **b** $F_x^0 = 1$; **c** $F_y^0 = 1$; **d** $M^0 = 1$

The data of coefficients η, λ_0, λ_1 and λ_2 (for λ_2, the right data are λ_{2S}) are summarized in Table 3. The calculation error of each coefficient (the deviation between model calculations and FEA results) is mostly less than 10% when the deformation is small (≤100μm), and the deformation of flexure hinges in compliant mechanisms for micro/nano positioning is generally very small. Further analyze Table 3, it can be found that the ratio t/R has a great influence on the calculation errors. As Fig. 9 summaries, for $t/R \in (0, 0.5)$, Δ_η (the calculation error of η) increases with t/R increasing, and its value is larger. The calculation errors Δ_{λ_0}, Δ_{λ_1}, Δ_{λ_2} and $\Delta_{\lambda_{2S}}$ of λ_0, λ_1, λ_2 and λ_{2S} have a similar trend, which decrease with t/R increasing and, past a minimum at $t/R = 0.25$,

then increase with t/R increasing. The finite element analysis shows the unified model calculations are precise for the right circular hinge when $t/R \in (0.2, 0.3)$.

Table 3 Model calculations and FEA results

t / mm	$\eta\left(10^{-6}\mathrm{m}\cdot\mathrm{N}^{-1}\right)$		$\lambda_0\left(\mathrm{m}^{-1}\cdot\mathrm{N}^{-1}\right)$		$\lambda_1\left(10^{-3}\mathrm{N}^{-1}\right)$		$\lambda_2\left(10^{-3}\mathrm{m}\cdot\mathrm{N}^{-1}\right)$		
	Model	FEA	Model	FEA	Model	FEA	Model		FEA
0.1	0.02409	0.02522	11.06	10.07	66.38	60.42	399.1	399.0	363.2
0.2	0.01694	0.01834	1.945	1.821	11.67	10.92	70.34	70.28	65.85
0.3	0.01378	0.01521	0.7025	0.6721	4.215	4.033	25.49	25.44	24.39
0.4	0.01190	0.01330	0.3409	0.3329	2.045	1.997	12.42	12.38	12.13
0.5	0.01061	0.01196	0.1946	0.1937	1.167	1.163	7.119	7.086	7.086
0.6	0.009655	0.01095	0.1231	0.1248	0.7385	0.7485	4.528	4.497	4.588
0.7	0.008912	0.01015	0.08362	0.08626	0.5017	0.5176	3.094	3.066	3.186
0.8	0.008309	0.009498	0.05986	0.06274	0.3592	0.3766	2.229	2.202	2.331
0.9	0.007808	0.008947	0.04460	0.04746	0.2676	0.2849	1.672	1.647	1.773
1.0	0.007382	0.008474	0.03430	0.03701	0.2058	0.2222	1.296	1.272	1.391

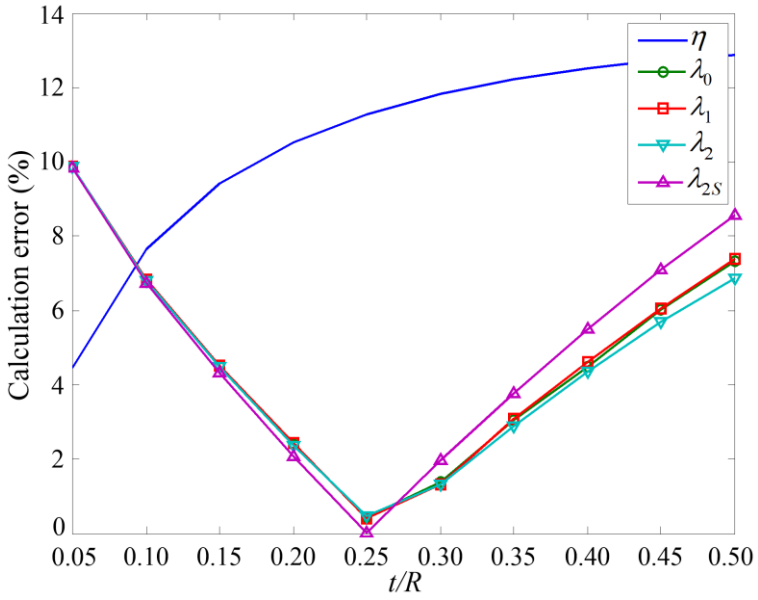

Fig. 9 The influence of t/R on calculation errors

Another set of finite element analysis simulations of a special combined hinge were performed to further investigate the overall size parameters influence on calculation error. The combined hinge consists of several right

circular hinge units (see Fig. 10), with the following parameters: $w=8mm$, $R=2mm$, $l_1=4mm$ and $t=0.5mm$. And the length L is changed by right circular hinge unit number n. As shown in Table 4, except that the calculation error of coefficient η is larger (approximately 11%), the calculation errors of coefficients λ_0, λ_1 and λ_2 don't exceed 0.5%, indicating the calculation error of the unified model is scarcely influenced by the unit number n.

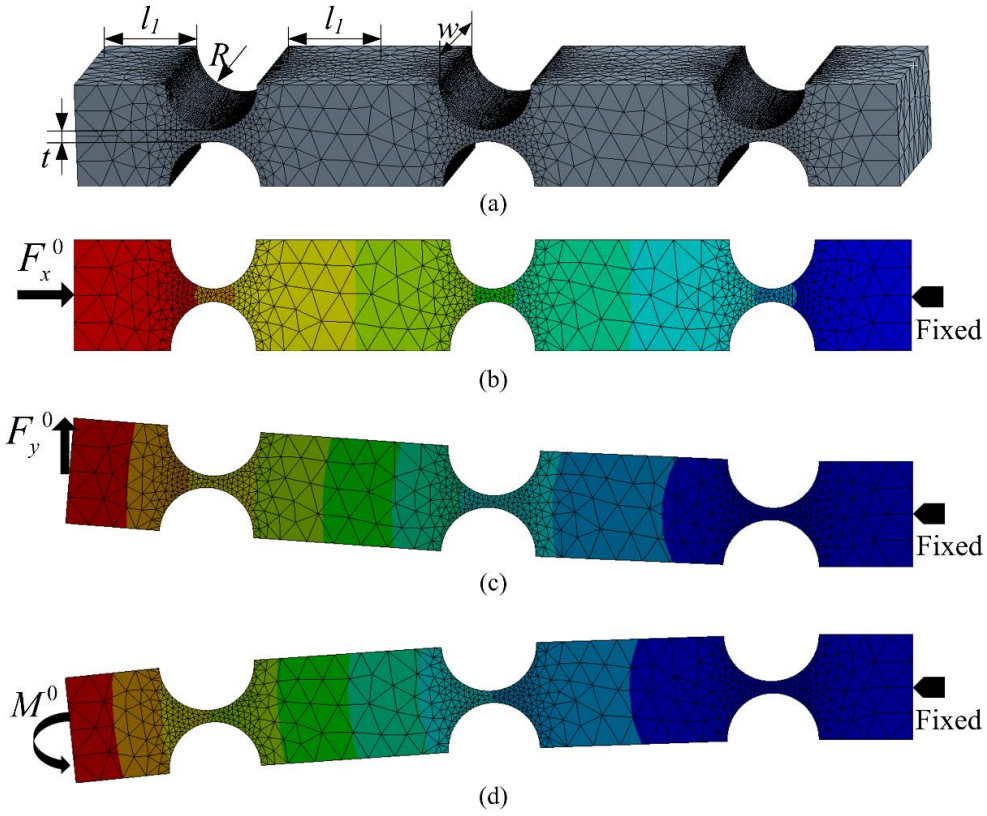

Fig. 10 FEA model of combined hinge: **a** Meshing model; **b** $F_x^0=1$; **c** $F_y^0=1$; **d** $M^0=1$

Table 4 Model calculations and FEA results

n	$\eta\left(10^{-6}\mathrm{m}\cdot\mathrm{N}^{-1}\right)$		$\lambda_0\left(\mathrm{m}^{-1}\cdot\mathrm{N}^{-1}\right)$		$\lambda_1\left(10^{-3}\mathrm{N}^{-1}\right)$		$\lambda_2\left(10^{-3}\mathrm{m}\cdot\mathrm{N}^{-1}\right)$		
	Model	FEA	Model	FEA	Model	FEA	Model		FEA
1	0.01061	0.01196	0.1946	0.1937	1.167	1.163	7.119	7.086	7.086
2	0.02122	0.02402	0.3891	0.3873	4.670	4.650	70.27	70.21	69.97
3	0.03183	0.03608	0.5837	0.5810	10.51	10.46	245.5	245.4	244.3
4	0.04244	0.04814	0.7783	0.7748	18.68	18.59	588.8	588.7	586.1
5	0.05304	0.06020	0.9728	0.9684	29.19	29.05	1156	1156	1151
6	0.06365	0.07226	1.167	1.162	42.03	41.84	2004	2004	1995

Further analyze the results in Table 4, as Fig. 11 pictures, the calculation error of η increases slightly with n increasing, indicating a slight error accumulation along the length. The calculation errors Δ_{λ_0}, Δ_{λ_1} and Δ_{λ_2} of λ_0, λ_1 and λ_2 are sustained at 0.45%, proving no error accumulations on length direction. In all, for the combine hinge, the calculation errors of the unified model coefficients are barely influenced by the unit number *n*, but mainly influenced by the geometric parameters of the right circular hinge unit, especially the ratio t / R.

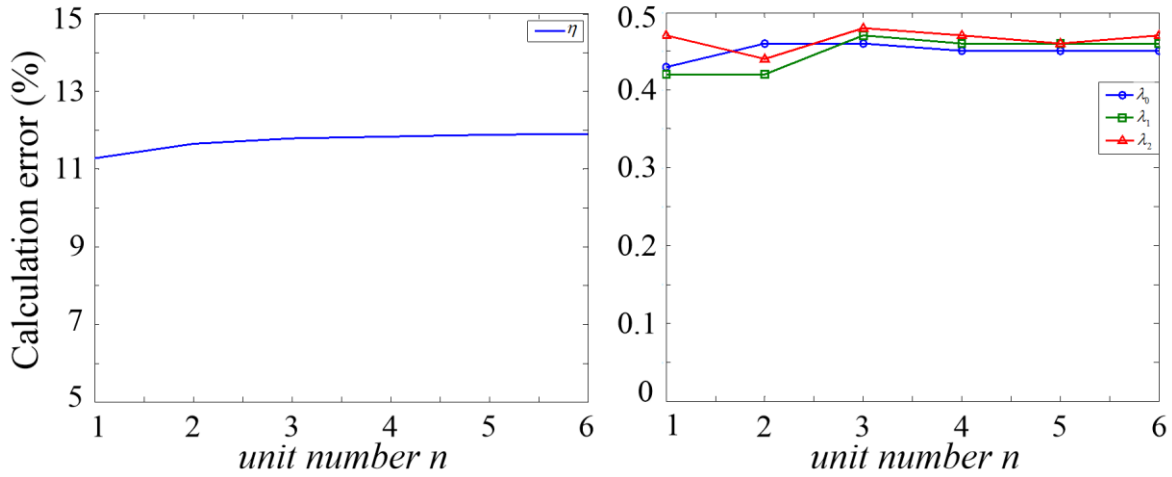

Fig. 11 Relationship between coefficient calculation error and n

4.2 Experimental testing

An experimental hinge sample was used to determine the deflection and slope caused by loads, compared with the calculations of the unified model, the pseudo-rigid-body method and finite element analysis. As Fig. 12 pictures, the hinge sample consists of two right circular sections and three constant section beams and its geometric dimensions are: $R = 2mm$, $t = 1mm$, $d_1 = 4mm$, $d_2 = 8mm$, $d_3 = 4mm$, $a = 0mm$, $b = 12mm$, and $c = 4.5mm$. The actual force F_y passing through the test point, can be seen as an equivalent force applied at the test point. The displacements v_1 and v_2 can be measured by laser displacement sensors S_1 and S_2 mounted at specific points (see Fig. 13). The slope and deflection at the test point can be calculated by geometry:

$$\begin{cases} \varphi = tan^{-1}\dfrac{v_2 - v_1}{b} \\ v = v_1 + c\left(sin\varphi\, tan\varphi + cos\varphi - 1\right) - a\, tan\varphi \end{cases} \tag{27}$$

Where v and φ are the deflection and rotation at the test point in Fig. 13.

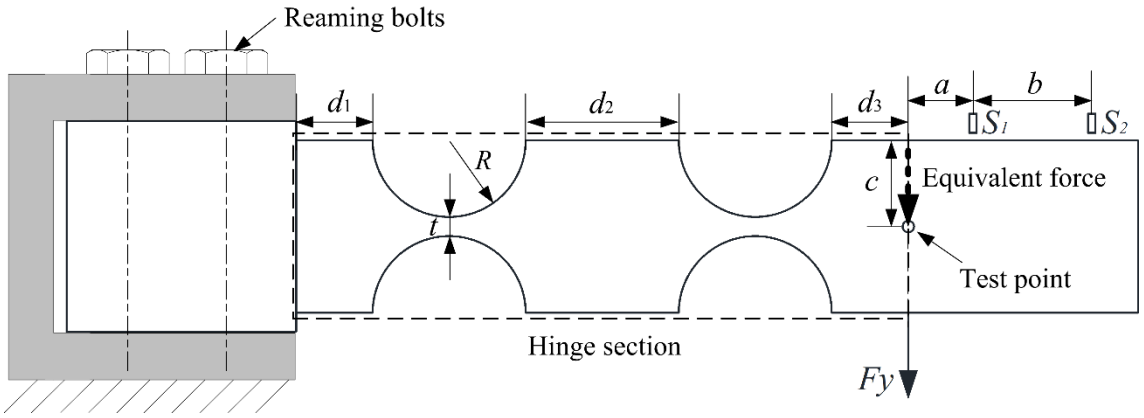

Fig. 12 Schematic representation of experimental setups

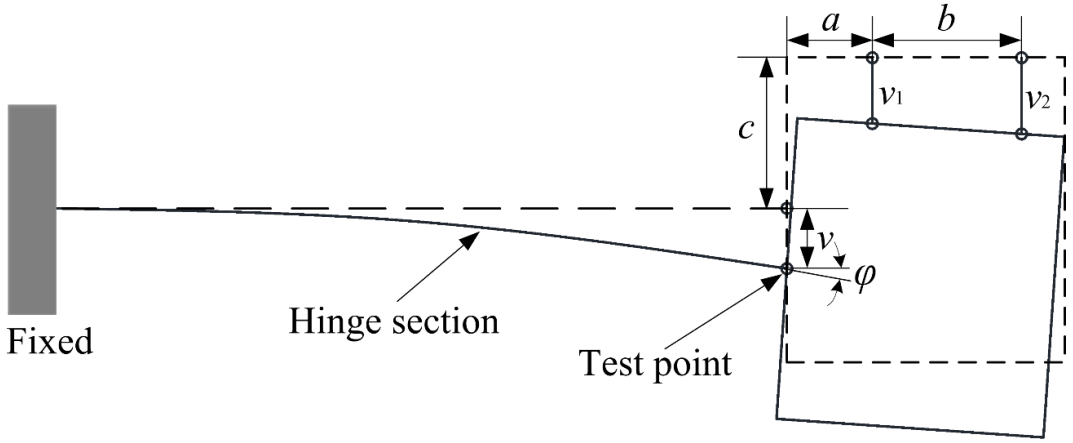

Fig. 13 Geometry of undeformed/deformed flexure hinge

The aluminum alloy specimen was precision-machined by a sheet $10.0mm$ thick. The material characterization of the specimen was: Young's modulus $E = 70GPa$ and Poisson's ratio $\mu = 0.33$. As Fig. 12 depicts, two reaming bolts were used to orient and constrain the specimen during experimental testing. A weight hanger was used to produce actual force F_y at the test point. And the load F_y increased from 0 up to $0.1gN$ in $0.01gN$ ($g = 9.801$) increments during testing. The zero positions of laser displacement sensors were set when the load $F_y = 0$, so the deflection caused by the selfweight of the coupons would not affect the experimental results. However, the slope caused by the

selfweight may influence the experimental results by changing the measurements v_1 and v_2. Considering the center of gravity and test points are not coincident, the gravity of the specimen can be seen as an equivalent force and a moment at the test point. By FEA, the slope caused by the selfweight can be obtained ($\Delta\varphi = 7.149\times10^{-5} rad$).

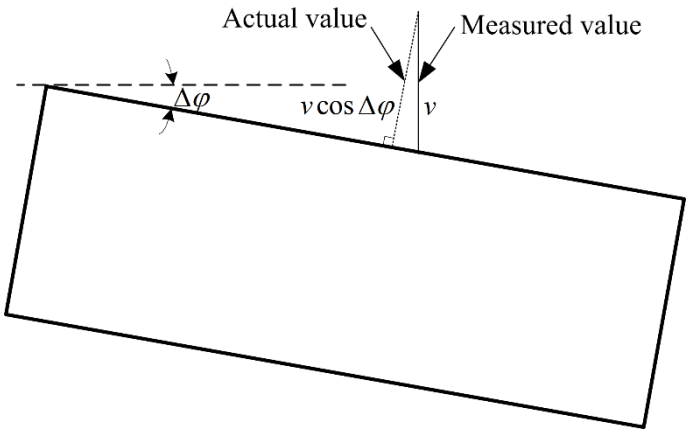

Fig. 14 Self-weight influence on experimental results

As Fig. 14 indicates, v represents the laser sensor's measured value, while $v\cos\Delta\varphi$ means the actual value under the selfweight. The relative error of the laser sensor's measured value can be expressed:

$$\left(v - v\cos\Delta\varphi\right)/v = \Delta\varphi^2/2 + o\left(\Delta\varphi^2\right) = 2.56\times10^{-9} \tag{28}$$

From Eq. (28), it can be seen that selfweight of the coupon has little effect on experimental results.

By the united element flexibility matrix model (Eq. (20)), the slope and deflection can be written:

$$\begin{cases} \varphi = \lambda_1 F_y \\ v = \lambda_2 F_y \end{cases} \tag{29}$$

The coefficients λ_1 and λ_2 can be derived by Eq. (12):

$$\begin{cases} \lambda_1 = \sum_{i=1}^{n} \int_{l_i} \dfrac{12x}{Ewt^3(x)} dx \\ \lambda_2 = \sum_{i=1}^{n} \int_{l_i} \dfrac{12x^2}{Ewt^3(x)} dx + \sum_{i=1}^{n} \int_{l_i} \dfrac{1.2}{Gwt(x)} dx \end{cases}, x \in (0, L) \tag{30}$$

Where the thickness function $t(x)$ can be expressed by geometry (Fig. 12):

$$t(x)=\begin{cases} 2R+t, x\in(0,d_1)\bigcup(2R+d_1,2R+d_1+d_2)\bigcup(4R+d_1+d_2,4R+d_1+d_2+d_3) \\ t+2R-2\sqrt{R^2-(R+d_1-x)^2}, x\in(d_1,2R+d_1) \\ t+2R-2\sqrt{R^2-(3R+d_1+d_2-x)^2}, x\in(2R+d_1+d_2,4R+d_1+d_2) \end{cases} \tag{31}$$

The slope and deflection at the test point can be also calculated by pseudo-rigid-body method (Slavisa et al. 2018).

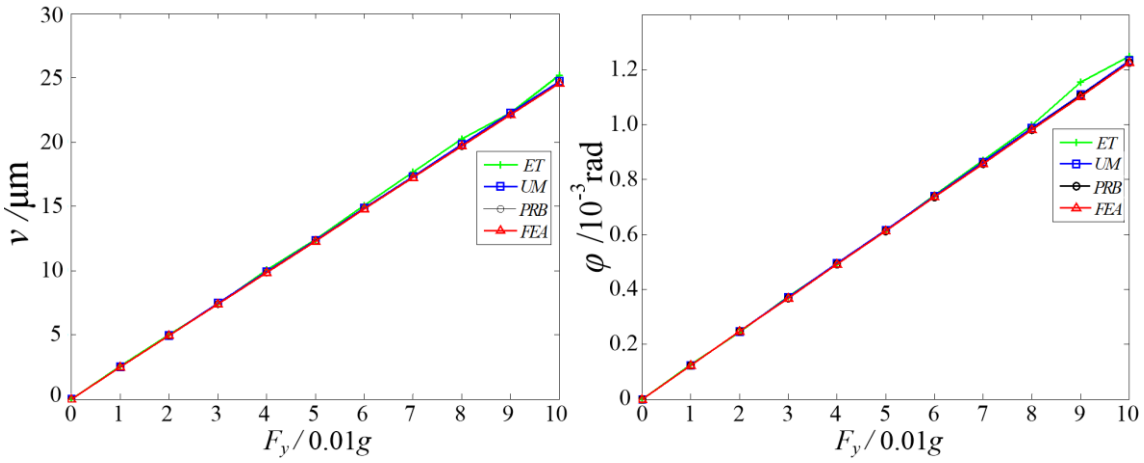

Fig. 15 The load-displacement curves

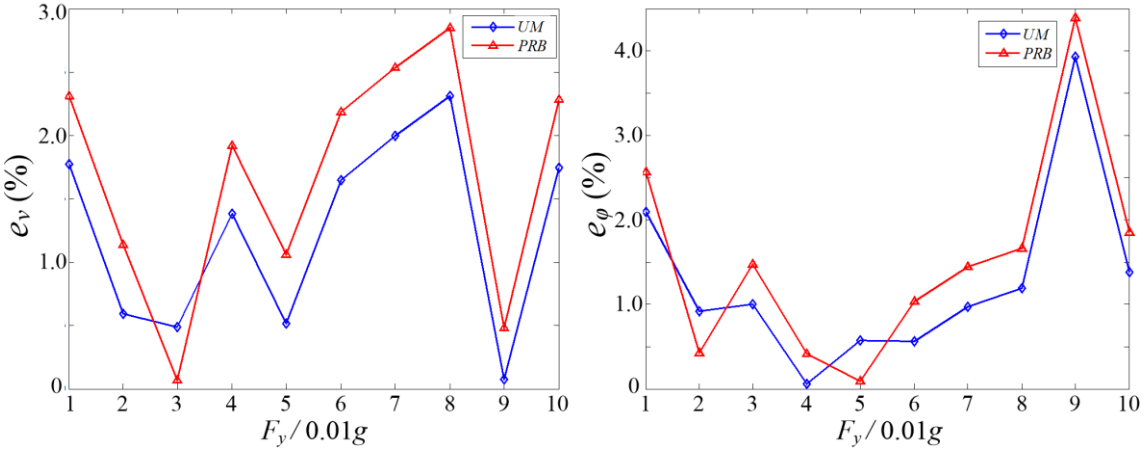

Fig. 16 The deviations between different methods and experimental results

Fig. 15 summarized all the results of experimental test (ET), unified model (UM), pseudo-rigid-body (PRB) and finite element analysis (FEA), showing the deviations between these methods is less than 5%. As Fig. 16 illustrates, comparing with PRB method, the deviations between UM and ET is less, indicating the proposed unified model considering the deflections of all parts of flexure hinge is more closed to reality.

5 Conclusions

Based on the principle of virtual work, this paper presents a unified element stiffness matrix model for variable cross-section flexure hinges in plane deformation with end loads and introduces four coefficients with curve integral, which simply and unify element stiffness matrices, providing a generalized and accurate solution to model the element stiffness matrices of flexure hinges in compliant mechanisms for micro/nano positioning.

In order to facilitate the applications of the unified element stiffness matrix model, it is employed in several common flexible hinges including constant cross section and right circular section, and shows good consistency with some results previously analyzed. In addition, finite element analysis and experimental testing were used to validate the proposed unified model and analysis the geometry influence on the unified model calculation precision. In addition, a specimen was machined for experimental testing. It is anticipated that the proposed unified element stiffness matrix model will be utilized in the design and optimization of planar-motion compliant mechanisms.

Acknowledgments This research is supported by National Natural Science Foundation of China (Grant nos. 51675376, 51675371, and 51675367), National Key R&D Program of China (nos. 2017YFB1104700, 2017YFE0112100, and 2016YFE0112100), China-EU H2020 FabSurfWAR (no. 644971) and MNR4SCell (no. 734174).

REFERENCES

Tian Y, Shirinzadeh B, Zhang D, Zhong Y (2010) Three flexure hinges for compliant mechanism designs based on dimensionless graph analysis. Precis Eng 34(1): 92-100

Qin Y, Shirinzadeh B, Zhang D, Tian Y (2013) Design and Kinematics Modeling of a Novel 3-DOF Monolithic Manipulator Featuring Improved Scott-Russell Mechanisms. J Mech Design 135(10): 101004

Wang F, Liang C, Tian Y, Zhao X, Zhang D (2016) Design and control of a compliant microgripper with a large amplification ratio for high-speed micro manipulation. IEEE-ASME T Mech 21(3): 1262-1271

Qi K, Xiang Y, Fang C, Zhang Y, Yu C (2015) Analysis of the displacement amplification ratio of bridge-type mechanism. Mech Mach Theory 87: 45-56

Bhagat U, Shirinzadeh B, Clark L, Chea P, Qin Y, Tian Y, Zhang D (2014) Design and analysis of a novel flexure-based 3-DOF mechanism. Mech Mach Theory 74(6): 173-187

Wang F, Ma Z, Gao W, Zhao X, Tian Y, Zhang D, Liang C (2015) Dynamic modeling and control of a novel XY positioning stage for semiconductor packaging. T I Meas Control 37(2): 177-189

Xiao X, Li Y, Xiao S (2016) Development of a novel large stroke 2-DOF micromanipulator for micro/nano manipulation. Microsyst Technol 23(7): 1-11

Guo Z, Tian Y, Tian J, Liu X, Wang F, Zhang H, Zhang D (2016) Probe system design for three dimensional micro/nano scratching machine. Microsyst Technol 23(6): 1-11

Cai K, Tian Y, Wang F, Zhang D, Shirinzadeh B (2016) Development of a piezo-driven 3-DOF stage with T-shape flexible hinge mechanism. Robot Cim-Int Manuf 37: 125-138

Wang F, Liang C, Tian Y, Zhao X, Zhang D (2016) A flexure-based kinematically decoupled micropositioning stage with a centimeter range dedicated to micro/nano manufacturing. IEEE-ASME T Mech 21(2): 1055-1062

Wang F, Liang C, Tian Y, Zhao X, Zhang D (2015) Design of a Piezoelectric-Actuated Microgripper With a Three-Stage Flexure-Based Amplification. IEEE-ASME T Mech 20(5): 2205-2213

Smith ST, Badami VG, Dale JS, Xu Y (1997) Elliptical flexure hinges. Rev Sci Instrum 68(3): 1474-1483

Lobontiu N, Paine JSN, Garcia E, Goldfarb M (2001) Corner-Filleted Flexure Hinges. J Mech Design 123(3): 346-352

Lin R, Zhang X, Long X, Fatikow S (2013) Hybrid flexure hinges. Rev Sci Instrum 84(8): 394-398

Chuan G, Chen Y, Tong G (2014) Element stiffness matrix for Timoshenko beam with variable cross-section. Chinese Journal of Computational Mechanics 31(2):265-272 (in Chinese)

Lignola G P, Spena F R, Prota A, Manfredi G (2017) Exact stiffness matrix of two nodes Timoshenko beam on elastic medium. An analogy with Eringen model of nonlocal EulerBernoulli nanobeams. Comput Struct 182: 556-572

Brown CJ (1984) Approximate Stiffness Matrix for Tapered Beams. J Struct Eng 110(12): 3050-3055

Marotta E, Salvini P (2018) Analytical Stiffness Matrix for Curved Metal Wires. Procedia Structural Integrity 8: 43-55

Long Y, Bao S (2000) Structural Mechanics Tutorial. I ed. China Higher Education Press

Lobontiu N (2014) Compliance-based matrix method for modeling the quasi-static response of planar serial flexure-hinge mechanisms. Precis Eng 38(3): 639-650

Noveanu S, Lobontiu N, Lazaro J, Dan M (2015) Substructure compliance matrix model of planar branched flexure-hinge mechanisms: Design, testing and characterization of a gripper. Mech Mach Theory 91: 1-20

Wang H, Zhang X (2008) Input coupling analysis and optimal design of a 3-DOF compliant micro-positioning stage. Mech Mach Theory 43(4): 400-410

Lobontiu N, Cullin M (2013) In-plane elastic response of two-segment circular-axis symmetric notch flexure hinges: The right circular design. Precis Eng 37(3): 542-555

Slavisa Salinic, Aleksandar Nikolic (2018). A new pseudo-rigid-body model approach for modeling the quasi-static response of planar flexure-hinge mechanisms. Mech Mach Theory 124: 150-161